Determination of strain rate dependence at intermediate strain rates using acceleration information

Ji-Min Kim[a], Jin-Seong Park[a,b], Do-Hyun Leem[a,c], Minki Kim[d], Frédéric Barlat[a], Fabrice Pierron[e,f], Jin-Hwan Kim[a*]

[a]GIFT, Pohang University of Science and Technology, San 31 Hyoja-dong, Nam-gu, Pohang, Gyeongbuk 790-784, Republic of Korea

[b]LG Chem, 104-1, Munji-dong, Yuseong-gu, Daejeon, Republic of Korea

[c]McCormick School of Engineering and Applied Science, Northwestern University, 2145 Sheridan Road, Evanston, IL 60208, United States

[d]Baker Systems Engineering, The Ohio State University, 1971 Neil Avenue, Columbus, OH 43210, United States

[e]Faculty of Engineering and Physical Sciences, University of Southampton, University Road, Southampton SO17 1BJ, United Kingdom

[f]MatchID NV, Leiekaai 25A, B-9000 Gent, Belgium

ABSTRACT

Precise stress-strain characteristics of materials for intermediate strain rates need to be utilized for analyzing various events in industry such as metal forging, sheet metal forming in manufacturing processes and automotive crash tests. However, the accurate evaluation of the load is not easy at intermediate or high strain rates, owing to the inertial effect. The present study aims at characterizing the hardening behavior using acceleration data without utilizing the load information with an application to a dual-phase DP980 steel sheet sample. Virtual measurements were obtained from a finite element model to check for the minimum acceleration magnitude necessary for stable identification. The same identification procedure as that used for the experiments was adopted. Also, a high-speed tensile testing equipment for steel sheet specimens was modified to increase the acceleration magnitude to implement the proposed methodology experimentally. The virtual fields

method was chosen as an inverse tool to determine the strain-rate dependence of the sheet metal specimens. The stress–strain curve of an advanced high-strength steel at intermediate strain rates obtained from the acceleration was compared with the curve from the load data, and promising results were obtained.

Keywords: Dynamic hardening behavior; Inverse identification; Digital image correlation; Intermediate strain rates; Sheet metal; Acceleration;

1. Introduction

Material behaviors at intermediate strain rates (5 s^{-1} ~ 500 s^{-1}) [1] have gained great interest to understand the mechanisms and predict the behaviors in various fields of industry such as metal forging, sheet metal forming in manufacturing processes [2,3] and automotive crash tests [4-6]. Stress-strain characteristic of materials at intermediate strain rates is the fundamental information to analyze such events.

Numerous experimental techniques have been developed to identify the strain-rate dependence at high rates of deformation since commonly, material properties change depending on the strain rate. Based on the method of experimentally generating dynamic conditions, high-speed test systems can be classified into several groups [7,8]: methods utilizing potential energy, such as the drop weight test, methods employing kinetic energy, such as the Taylor impact test, split Hopkinson pressure bars using kinetic energy and stress wave propagation, and servo-hydraulic machines. Among those, high-speed servo-hydraulic test machines have been widely used to obtain stress–strain curve information at various intermediate strain rates [9].

Nonetheless, the dynamic strain-hardening behavior of metallic materials at intermediate or high strain rates is not characterized easily since the precise measurement of the applied load is difficult owing to the effect of inertia [10]. Stress waves are produced at high strain rates, inducing high acceleration magnitudes. This results in the ringing problem in load cells of standard test machines [11].

Consequently, numerous studies have been conducted to mitigate the load-ringing phenomenon. Researchers have primarily focused on investigating three approaches. The first involves directly acquiring the load from a dogbone specimen by bonding strain gauges to its gripped section which deforms elastically [9,12]. The second is to increase the natural frequency of a jig part between the load cell and the specimen [11]. The final approach is to develop a load sensor by applying strain gauges to lightweight grips [9,13,14] because the ringing can be significant if the mass of the part between the specimen and the load cell is large [15].

Alternatively, several attempts have been made to determine material parameters at high rates using acceleration information instead of load data. The idea is to use the acceleration field as an embedded load cell through the dynamic equilibrium equation, provided that full-field displacements are available experimentally with sufficient temporal resolution to accurately derive accelerations. Moulart et al. [16], Pierron and Forquin [17], and Pierron et al. [18] used this concept to identify the elastic moduli of concrete [17] and composite [16,18] specimens. They used the grid method [19] as a full-field measurement technique to measure the strain and acceleration fields, in combination with the virtual fields method (VFM) [20] as an inverse method to identify material parameters at high rates. The VFM is an inverse identification method for acquiring the constitutive parameters following the principle of virtual work.

In addition, the VFM was used for elasto-plastic cases to characterize dynamic behaviors using only the acceleration information without acquiring the load [21-24].

Recently, several studies tried to calibrate the rate-dependent hardening properties from strain and acceleration fields adopting the image-based inertial impact (IBII) test [18]. For elasto-plasticity, the test is akin to a Taylor impact test but with a flat plane stress specimen. Bouda et al. [23] optimized the IBII test to characterize the dynamic behavior of titanium at high rates by optimizing the specimen geometry through a computational approach. Fourest et al. [24] retrieved the parameters of a Johnson–Cook model for a titanium alloy. Linear and Voce hardening parameters at different strain rates were identified for stainless steel from nonhomogeneous strain-rate data in Fletcher et al. [25].

However, the target strain rates in the above studies were very high (up to 3,000 s^{-1}) and not in the intermediate range. The objective of this study is to identify the dynamic hardening parameters at intermediate strain rates for thin steel sheet material by using acceleration rather than load cell data. The VFM was adopted in this study as an inverse tool to retrieve the strain-rate dependence of the sheet metal specimens. The idea of determining the strain rate dependence for various strain rates comes from the observation that the strain rate distribution is heterogeneous over the area of interest (AOI) [27]. This means that sufficient strain rate information can be fed into the VFM to retrieve the strain rate dependence with a proper rate dependent model. FE simulations were performed using the Abaqus software to check the minimum acceleration required because Leem et al. [26] revealed that a critical magnitude of acceleration is necessary for identification using the VFM. Subsequently, a high-speed tensile equipment for sheet metal specimens [27] was modified to increase the acceleration based on the observations from the FE simulation. Several aspects of the modification were closely investigated to optimize the configuration of the tester and specimen. The digital image correlation (DIC) technique was applied to calculate the displacement, strain, strain rate, and acceleration during the experiments using a high-speed camera. Then, identification using the VFM with the Johnson–Cook rate-dependent model was performed from the measured quantities. Finally, some features of the test results are discussed.

2. Methodology

2.1 Impact frame high-speed (IFHS) tensile equipment

A new type of high-speed tensile test equipment for steel sheet specimens on the basis of the work of Tran and Kim [28] was manufactured [27]. Views of the experimental equipment are presented in Fig. 1 and the testing principle is shown in Fig. 2. Unlike typical impact testing systems that utilize potential or kinetic energy, this one uses the elastic strain energy stored in frame bars to generate high-speed impact pulses. Two frame bars are linked to a hydraulic pump using a coupler. The coupler is in the form of a cylinder with a notch at the center; therefore, the coupler breaks when a critical amount of load is applied. Once the pump applies a tensile force to the coupler, it sustains the load up to a critical value of load as shown in Fig. 2(a). In the meanwhile, the frame bars accumulate elastic strain energy simultaneously. If the load is high enough to fracture the coupler as shown in Fig. 2(b), the elastic strain energy stored in the frame bars is converted to kinetic energy to draw the steel sheet specimen attached to the frame parts in tension at a high strain rate, as shown in Fig. 2(c). In addition, photoelectric sensors (transmitter and receiver) are located at both sides of the coupler as a trigger system in Fig. 1. This trigger system sends a signal to the high-speed camera when the coupler breaks so that the high-speed camera can capture deformation images. Adjusting the designs of the frame bars and the coupler can change the strain rate.

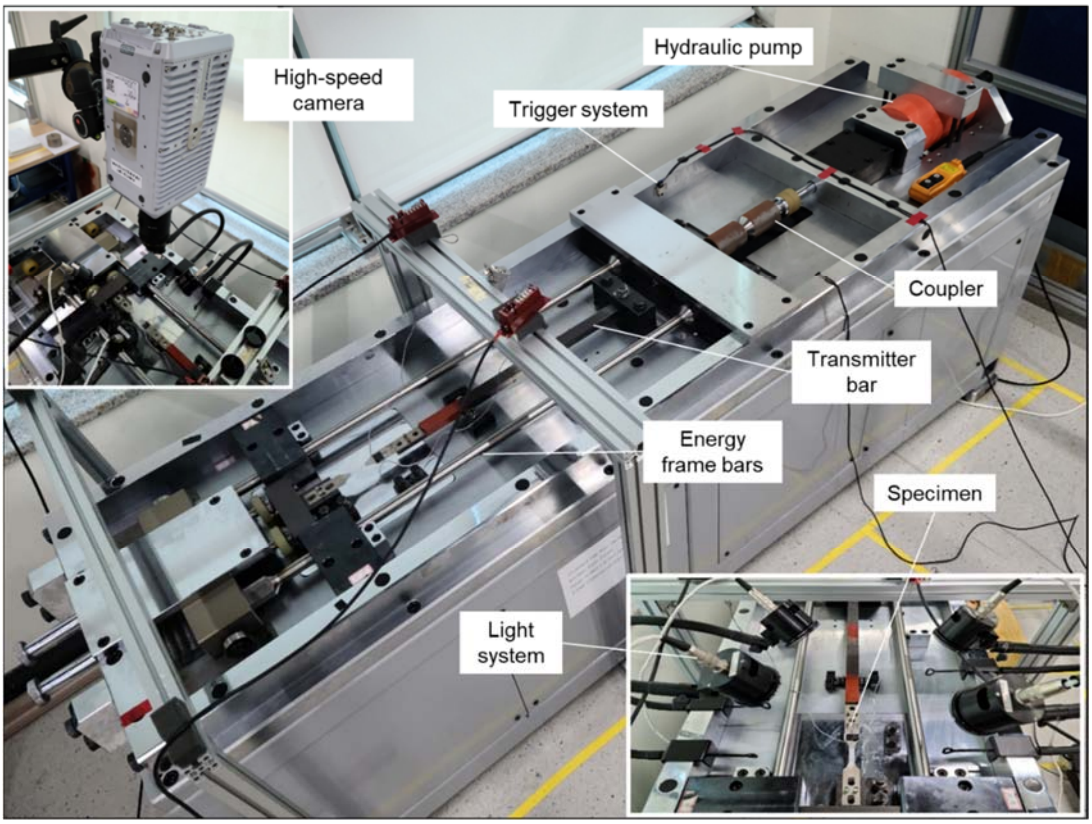

Fig. 1. Views of the IFHS tester.

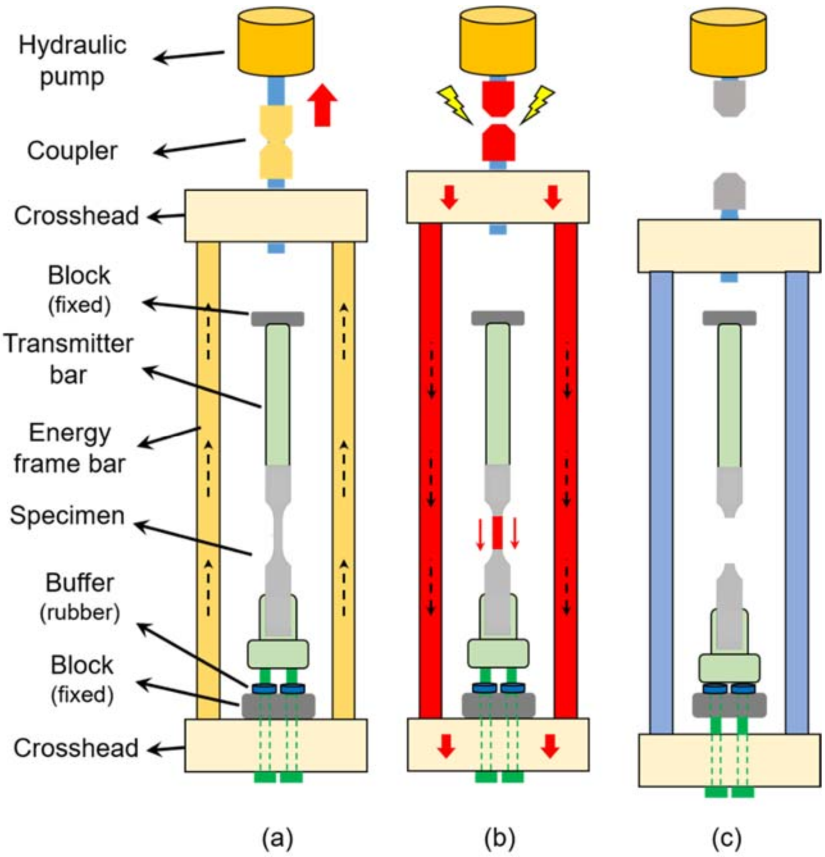

Fig. 2. The principle of the IFHS tester.

A dogbone test specimen was designed for the experiments, as depicted in Fig. 3. The specimen has circular holes on one grip end, and rounded rectangles on the other end. The left-hand side with the rounded rectangles acts as a slack adaptor, allowing the movable part to the left to gather enough speed before the load is transmitted to the specimen. In this study, a dual-phase DP980 steel sheet specimen with 1.2 mm thickness was chosen.

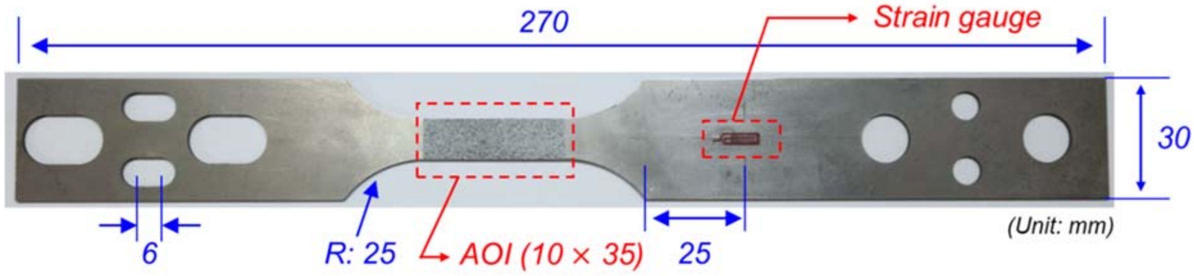

Fig. 3. Geometry of specimen for the IFHS tests (unit: mm).

2.2 Full-field measurements with DIC technique

A speckle pattern was sprayed with black paint on the area of interest (AOI) of steel sheet specimens initially covered with white paint for the DIC analysis [29]. The speckle pattern images were captured using a high-speed camera at 120,000 frames per second (fps) during the high-speed tensile tests. The size of the AOI was 35 mm (initial gauge length) × 10 mm (width), sampled by 640 × 128 pixels. Vic-2D software from Correlated Solutions was utilized for the DIC calculation. Information on the imaging and DIC parameters is provided in Table 1, according to the recommendations of Jones and Iadicola [30]. The red dots in the AOI (Fig. 4) represent the measured DIC points.

In order to calculate the logarithmic strain and acceleration fields to be used for determination of strain-rate dependence using the VFM, the exact AOI dimension was obtained from a FE software and the whole AOI was meshed using triangular elements as shown in Fig. 4.

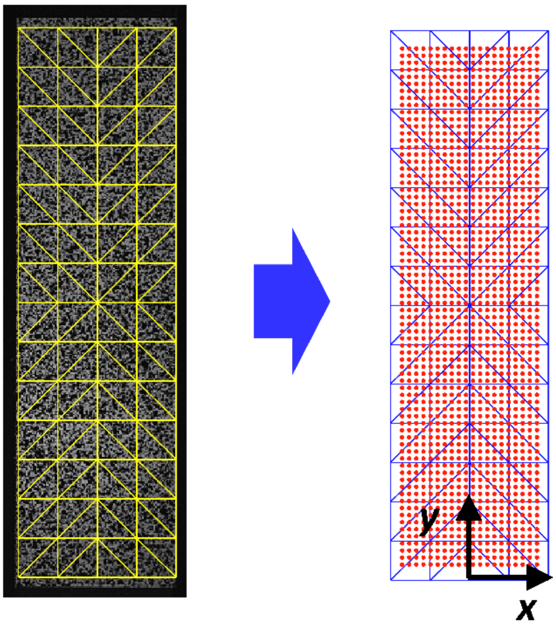

Fig. 4. Speckle patterns in the AOI and measured DIC points (*y* and *x* indicate the rolling and transverse directions, respectively).

Based on the known coordinates of each triangle nodes and of the measured DIC points inside each triangle in the undeformed configuration, the mapping which projects the measured DIC points onto the nodal points can be calculated using a basis of piecewise linear functions [31] as adopted in the FE method [32]. This procedure is conducted by linear interpolation (least-squares fitting). Next, the nodal coordinates of each triangle in the deformed configuration at each loading stage are approximated from the coordinates of measured DIC points in the deformed configuration by applying the piecewise functions. The relationship between the deformed DIC points and the deformed nodal points can be expressed as:

$$\{\bar{\mathrm{x}}\} = [\Phi]\{\bar{\mathrm{X}}\} \tag{1}$$

where $\{\bar{\mathrm{x}}\}$ is the location vector of the measured DIC points, $[\Phi]$ the matrix of the piecewise linear functions and $\{\bar{\mathrm{X}}\}$ the location vector of nodal points. Then, the location vector of nodal points can be obtained using the explicit direct solution to the least squares minimization problem [32]:

$$\{\bar{\mathrm{X}}\} = ([\Phi]^T[\Phi])^{-1}[\Phi]^T\{\bar{\mathrm{x}}\} \tag{2}$$

This fitting process has the advantage of allowing for the reconstruction of data up to the specimen edges, which is critical for the VFM. In addition, the fitting process has an effect of spatial smoothing to reduce the experimental noise.

Next, the linear relationship between the nodal coordinates of each triangle in the undeformed and deformed configuration can be calculated using a 2D affine transformation:

$$x_d = a_1 + a_2 X_u + a_3 Y_u, \qquad y_d = a_4 + a_5 X_u + a_6 Y_u \tag{3}$$

where x_d, y_d are nodal coordinates in the deformed configuration and X_u, Y_u nodal coordinates in the undeformed configuration. The six coefficients ($a_1 \sim a_6$) for each triangle can be obtained from six equations (two equations per node and total three nodes). Finally, the deformation gradient F in each triangle is calculated by Eq. (4) assuming a plane stress and the incompressibility in plasticity (det (F) = 1).

$$\mathrm{F} = \begin{bmatrix} \frac{\partial x}{\partial X} & \frac{\partial x}{\partial Y} & 0 \\ \frac{\partial y}{\partial X} & \frac{\partial y}{\partial Y} & 0 \\ 0 & 0 & \frac{1}{\frac{\partial x \partial y}{\partial X \partial Y} - \frac{\partial x \partial y}{\partial Y \partial X}} \end{bmatrix} = \begin{bmatrix} a_2 & a_3 & 0 \\ a_5 & a_6 & 0 \\ 0 & 0 & \frac{1}{a_2 a_6 - a_3 a_5} \end{bmatrix} \tag{4}$$

Now, the logarithmic strain tensor ε_{ln} is calculated from the deformation gradient F through the right stretch tensor U $(U^2 = F^T F)$ as in Eq. (5).

$$\varepsilon_{ln} = \sum_{i=1}^{3} \ln(\lambda_i) r_i \otimes r_i \tag{5}$$

where λ_i and r_i are the eigenvalues and eigenvectors of the right stretch tensor U respectively.

The strain rate $\dot{\varepsilon}$ in each triangular element at each time step is calculated from the obtained logarithmic strain. In the rest of manuscript, "AOI-averaged" indicates the average of values in all triangular elements.

$$\dot{\varepsilon}_i \left(t + \frac{\Delta t}{2} \right) = \frac{\varepsilon_i(t + \Delta t) - \varepsilon_i(t)}{\Delta t} \tag{6}$$

where ε indicates strain, i corresponds to x, y, or xy and t represents time. Also, the displacement u can be derived at the centroid of each triangle because the nodal coordinates of each triangle in the undeformed and deformed configuration are known. Then, the velocity v and the acceleration a in each triangular element are obtained at each time step from the measured displacement u by simple finite difference and second order finite differences, respectively.

$$v_j\left(t+\frac{\Delta t}{2}\right)=\frac{u_j(t+\Delta t)-u_j(t)}{\Delta t} \tag{7}$$

where j can be either x or y.

$$a_j(t)=\frac{u_j(t+\Delta t)+u_j(t-\Delta t)-2u_j(t)}{\Delta t^2} \tag{8}$$

In order to calculate the strain and acceleration resolution (the smallest value which can be detected above the noise), 21 successive speckle pattern images were obtained at rest using a high-speed camera at 120,000 fps. Then, the logarithmic strain and acceleration were derived as described above and the standard deviation values of the obtained logarithmic strain and acceleration in the triangle elements were calculated. The information of strain and acceleration resolution is presented in Table 1.

Table 1

Information on the DIC technique (DP980).

Camera	Photron FASTCAM SA-X2
Sensor and digitization	1024 × 1024 pixels, 12-bit
Lens, imaging distance	Sigma 105 mm Macro Lens, 390 mm
Total image number (recording time)	54 (0.45 ms)
Frame rate	120,000 fps
Image resolution (in pixel size)	640 × 128
Conversion of pixel-to-mm	1 pixel = 0.089 mm
Subset and its offset (step)	21, 5 pixels
Interpolation, shape functions, correlation criterion	Cubic spline, affine, Normalized squared differences
Strain smoothing technique	Linear shape functions (triangular finite element)
Strain resolution	1.21×10^{-5} (ε_{xx}), 1.67×10^{-5} (ε_{yy}), 7.29×10^{-5} (ε_{xy})
Acceleration resolution	3.54 km/s^2 (a_{xx}), 3.62 km/s^2 (a_{yy})

2.3 Constitutive model

An elasto-plastic constitutive model that can properly capture the dynamic strain-hardening behavior is required. In this research, the plane stress von Mises yield criterion and the Johnson–Cook model for a rate-dependent hardening law were taken because the flow stress of steels depends on the strain rate. In particular, advanced high-strength steels (AHSSs), prominent in automotive applications, tend to exhibit a larger flow stress at higher strain rates [33]. The classical associated flow rule was assumed.

The yield condition can be expressed as

$$f(\sigma, \varepsilon_p) = \sigma_{eq}(\sigma) - \sigma_s(\varepsilon_p) = 0 \tag{9}$$

where σ_{eq} denotes the von Mises equivalent stress, σ_s denotes the current flow stress, and ε_p denotes the equivalent plastic strain.

The Johnson–Cook model has quasi-static and dynamic terms,

$$\sigma_s = \sigma_r \left\{1 + C \ln\left(\frac{\dot{\varepsilon}_{p,d}}{\dot{\varepsilon}_{p,r}}\right)\right\} \tag{10}$$

where σ_r and $\dot{\varepsilon}_{p,r}$ indicate the stress and reference equivalent plastic strain rate in quasi-static condition, respectively, and $\dot{\varepsilon}_{p,d}$ is the equivalent plastic strain rate in dynamic condition. $\sigma_r(\dot{\varepsilon}_{p,r})$ can be any hardening law. The strain-rate sensitivity C is a constant in the Johnson–Cook model.

In this study, the hardening parameters of σ_r are obtained from quasi-static uniaxial tensile tests, and the dynamic parameter C is calibrated with the VFM using acceleration data from intermediate-strain-rate experiments to lower the parameter numbers to be determined using the VFM.

2.4 The virtual fields method (VFM)

In this research, the virtual fields method (VFM) was chosen as an inverse identification scheme to determine the Johnson–Cook material parameter C. The VFM uses the principle of virtual work, which indicates the global equilibrium condition. The equilibrium equation in dynamic elasto-plasticity can be presented as follows (in the absence of body forces):

$$-\int_V \left[\int_0^t \frac{d\sigma_{ij}}{dt} dt\right] \varepsilon_{ij}^* dV + \int_{S_f} T_i u_i^* dS = \int_V \rho a_i u_i^* dV \tag{11}$$

where $d\sigma/dt$ is the stress rate tensor, V the measured volume, T the force distribution applied on the specimen boundary S_f, ε^* the virtual strain field obtained from the virtual displacement field u^*, ρ the density, and a is the acceleration. The summation convention is applied to repeated indices.

The equilibrium equation describes that the external virtual work (EVW) from the surface tractions T is equal to the sum of the acceleration virtual work (AVW) due to the acceleration a and the internal virtual work (IVW) due to the stress. The AVW is negligible during quasi-static conditions but should be included in the VFM identification at high rates, since the acceleration effects cannot be neglected.

The entire loading history needs to be considered for the identification of the elasto-plastic behavior. An iterative procedure is needed to minimize the difference between the (EVW $-$ AVW) and IVW at each deformation step [34]. The stress increments were calculated repeatedly at each time step until the virtual work gap was minimized. The radial return algorithm suggested by Sutton et al. [35] was used for stress calculation. The nonlinear least squares algorithm in MATLAB was utilized for the optimization.

In order to conduct the optimization to extract the dynamic parameter, suitable virtual fields must be selected. The virtual displacement fields need to be continuous and piecewise differentiable across the AOI. Two approaches were adopted to identify the parameter C of the Johnson–Cook model in this study. The first was to use the acceleration data without load, and the second was to utilize the load data only for the validation of the results obtained using the acceleration. Therefore, two sets of virtual fields were chosen for each case. The first set of virtual fields for acceleration is given by Eq. (12). In this case, u^* is chosen to eliminate the effect of the EVW term during the iteration.

$$u^*_{1\mathrm{x}} = 0,\ u^*_{1\mathrm{y}} = (y - y_{min})(y - y_{max}) \tag{12}$$

where x and y denote the coordinates in the horizontal and vertical directions, respectively, as shown in Fig. 4. The second set of virtual fields for the load is given by Eq. (13).

$$u^*_{2\mathrm{x}} = 0,\ u^*_{2\mathrm{y}} = y \tag{13}$$

It should be noted here that regarding the VFM identification using the load data and the second set of virtual fields for the validation, the same identification scheme adopted in Park et al. [27] will be used for the rest of this study.

3. FE simulation

The specific goal of the FE simulation was to verify the VFM identification routines of the Johnson–Cook parameter using acceleration, and to find the minimum acceleration magnitude required for the identification. Virtual measurement data was obtained using the FE program Abaqus/Explicit. The same identification procedure used for the experiments was applied as well in this case.

3.1 FE model

An FE model according to the real geometry with the 1.0 mm thick specimen was built, as presented in Fig. 5. To imitate measured DIC points, four-node shell elements (S4R) and a fine mesh size (0.3 mm) were chosen. The AOI was selected to be the central area with a 35 mm gauge length and meshed as described in Section 2.2. The virtual measurement data was obtained at uniformly spaced time intervals (100 time steps). From each triangular element, the strain and acceleration were calculated at each time step. The load was measured using the reaction force acting on the bottom edge, as shown in Fig. 5. Table 2 lists the simulation conditions used in this study.

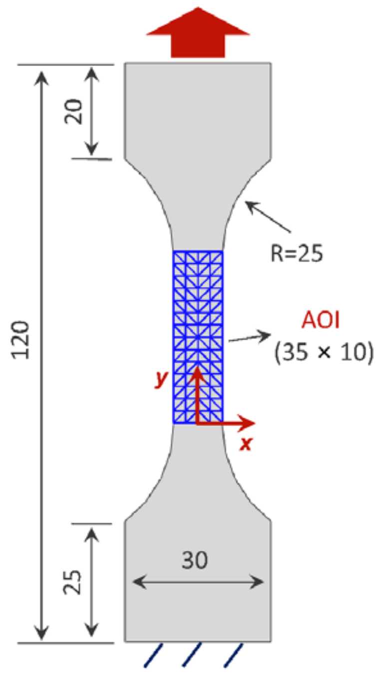

Fig. 5. Model for the dynamic FE simulations (unit: mm, upper edge: velocity boundary condition & U_x=0, bottom edge: U_x=U_y=0).

Table 2

Detailed information for the FE simulation.

Analysis mode	Abaqus / Dynamic Explicit		
Element type	Four-node shell quadrilateral element (S4R)		
Mesh size	0.3 mm		
Boundary condition	Velocity boundary condition		
Simulated time	0.47 ms		
Step number	100 steps		
Rate-dependent hardening law	Swift + Johnson–Cook $X_1(X_2+\varepsilon_p)^{X_3}\left(1+C\ln\left(\frac{\dot{\varepsilon}_{p,d}}{\dot{\varepsilon}_{p,r}}\right)\right)$		
Material properties			
X_1, X_2, X_3 (MPa)	1430	0.0021	0.157
C	0.03		
$\dot{\varepsilon}_{p,r}$ (s^{-1})	0.001		
Elastic modulus	200 GPa		
Poisson's ratio	0.3		
Density	7,800 kg/m^3		

To mimic the real loading conditions in the experiments, the velocity of the specimen pulling side during the IFHS tensile test was applied as boundary condition to the FE model [27], as shown in Fig. 6 as 'original'. × 0.8, × 0.65 and × 0.55 correspond to faster loading ramps, this will be explained later.

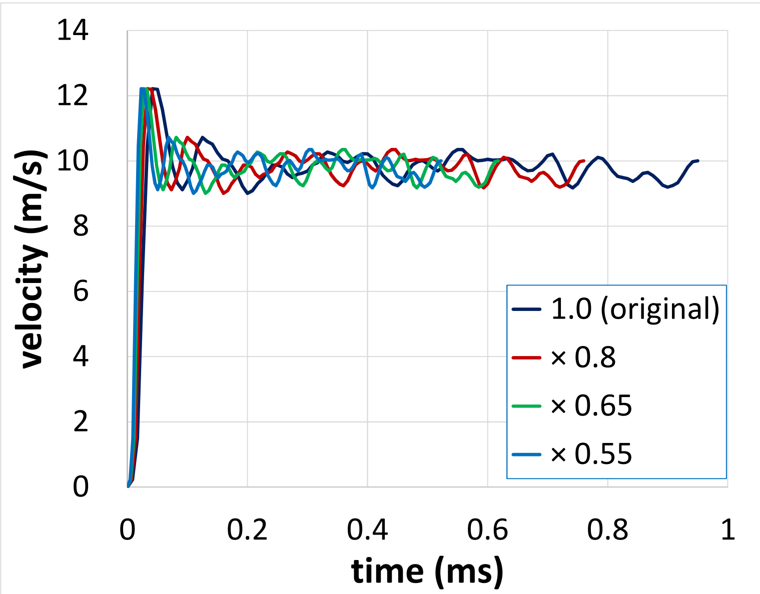

Fig. 6. Velocity boundary conditions.

3.2 VFM validation with the Johnson–Cook model

The built-in Johnson–Cook model in Abaqus was used. The input coefficients chosen for the FE simulations are listed in Table 2. For the quasi-static flow stress σ_r in Eq. (10), the Swift model in Eq. (14) was selected

$$\sigma_r = X_1 \left(X_2 + \varepsilon_p \right)^{X_3} \tag{14}$$

in which the coefficients were set to known values for the identification.

The dynamic parameter C only was determined using acceleration as listed in Table 3. The relative error of the identified Johnson–Cook model parameter C was 49.3 % (original elapsed time condition), which led to a large difference with the reference target flow curve determined at 200 s^{-1} strain rate as presented in Fig. 7. However, the identified result was similar to the input value when the parameter was evaluated using load information [27].

Table 3

Maximum acceleration magnitude and determined Johnson–Cook parameter using acceleration for each case (FE simulation, R.E.: relative error).

Elapsed time condition	Maximum acceleration magnitude (km/s^2)	Input	Identified	R.E. (%)
1.0 (original)	463.3	0.03	0.0152	49.3
× 0.8	749.8		0.0285	5.00
× 0.65	981.3		0.0304	-1.33
× 0.55	1147		0.0303	-1.00

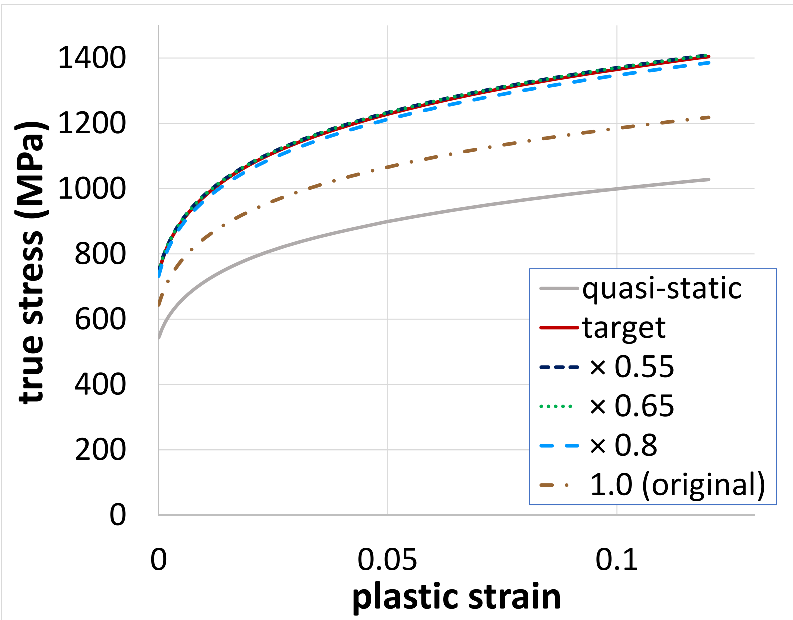

Fig. 7. Stress–strain curve comparison between the identified results using acceleration and the input at 200 s^{-1} strain rate.

A previous study [26] conducted an FE analysis and observed that a minimum threshold of acceleration magnitude was required for proper identification using the VFM. One of the purposes of the simulation in this study was to check the minimum acceleration magnitude required for the VFM identification. Therefore, the total testing time was decreased by 0.8, 0.65, and 0.55 times to increase the magnitude of the acceleration while maintaining the magnitude of the velocity, as shown in Fig. 6. Subsequently, the new velocity boundary conditions were fed to the FE simulations, and the same identification processes were repeated.

The maximum acceleration magnitude and the evolution of the AOI-averaged acceleration for each case are presented in Table 3 and Fig. 8.

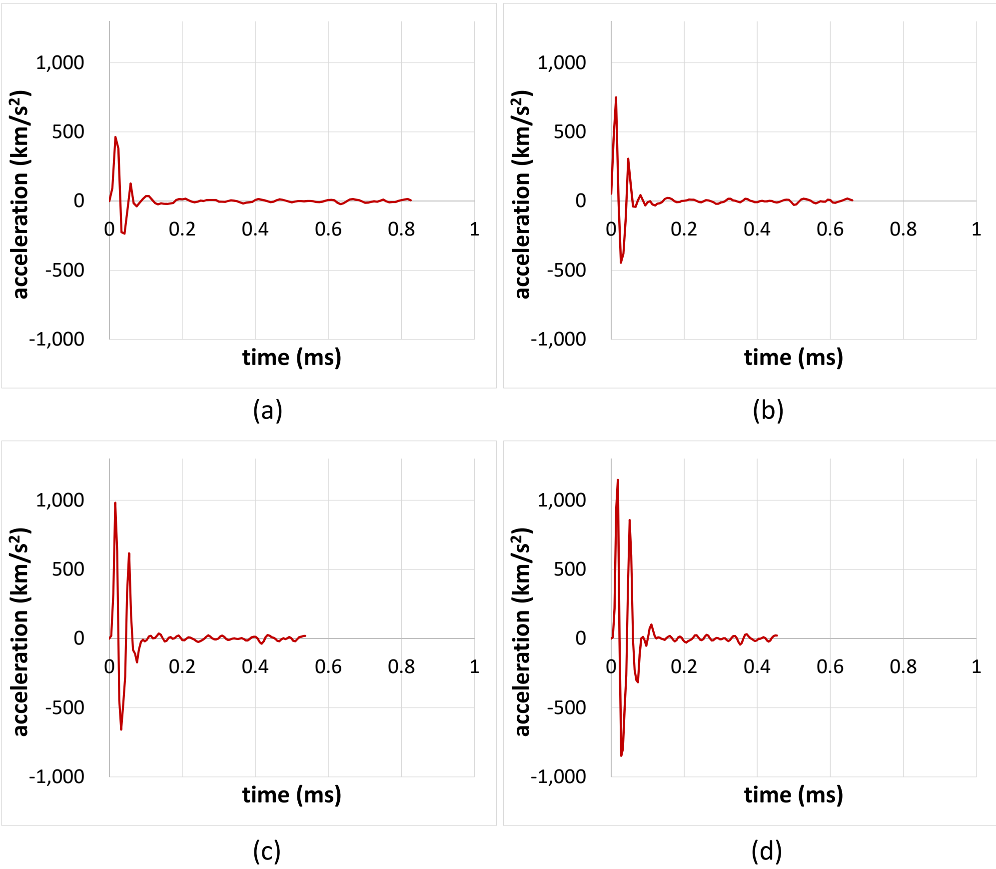

Fig. 8. AOI-averaged acceleration evolution: (a) 1.0 (original), (b) × 0.8, (c) × 0.65, and (d) × 0.55.

The different velocity boundary conditions resulted in different elongations as shown in Fig. 9. The obtained maximum engineering strains are 0.211, 0.164, 0.128 and 0.108 for 1.0 (original), × 0.8, × 0.65 and × 0.55, respectively where the engineering strain at maximum strength is 0.125. Therefore, it is considered that strain level is appropriate for the identification of Johnson–Cook parameter for all the cases.

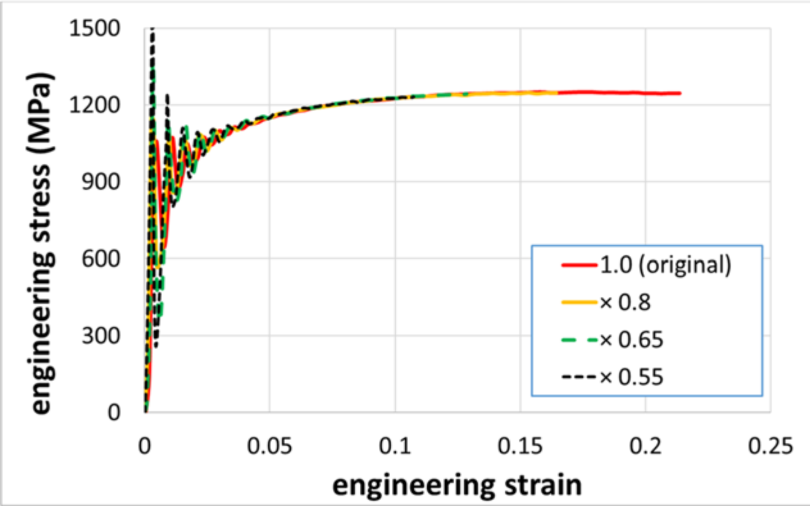

Fig. 9. Engineering stress-strain curves obtained from different boundary conditions.

The relative errors of the determined parameters in Johnson–Cook model and the corresponding calculated flow stresses at a strain rate of 200 s^{-1} are presented in Table 3 and Fig. 7, respectively. The Johnson–Cook model parameter was correctly identified using the acceleration only when the maximum acceleration magnitude was approximately 1.0×10^3 km/s^2 (× 0.65 times). Although the parameter obtained with this acceleration (× 0.65 times) was slightly under-predicted (-1.33 %), the difference in flow stress was less than 1 %.

In addition, the evolution of the AOI-averaged strain rate and measured load in the loading direction (reaction force from the bottom edge in Fig. 5) for the × 0.65 elapsed time condition are shown in Fig. 10.

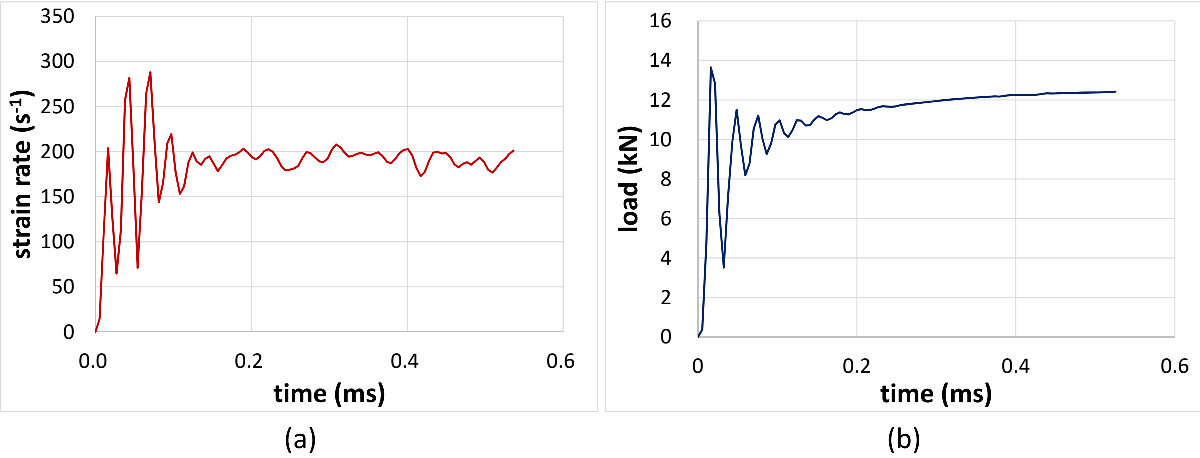

Fig. 10. Evolution of (a) AOI-averaged strain rate (b) load in the loading direction (FE simulation, × 0.65 elapsed time condition).

4. Experiment

4.1 Modification of IFHS tester to increase acceleration

As the current study aimed to determine the dynamic properties from acceleration, the magnitude of acceleration in the IFHS experiments should be sufficiently high to provide information for identification. Thus, several methods have been considered and applied to increase the acceleration magnitude.

4.1.1 Modification of grip condition

As shown in Fig. 11, the grip condition was revised in the current test setup [27]. For the ordinary circular holes, the specimen is pulled in tension from the start with the strain rate increasing gradually during deformation but, this configuration diminishes the initial acceleration. Since, the original circular holes are unsuitable for providing a sudden deformation jump, special attention was paid to modifying the grip conditions. The specimen must initiate its deformation after the pulling mechanisms reach a certain speed, which was achieved by replacing the circular holes with rounded rectangles, as shown in Fig. 11. The sliding distance for the modified specimen with rounded rectangles was set to 6 mm.

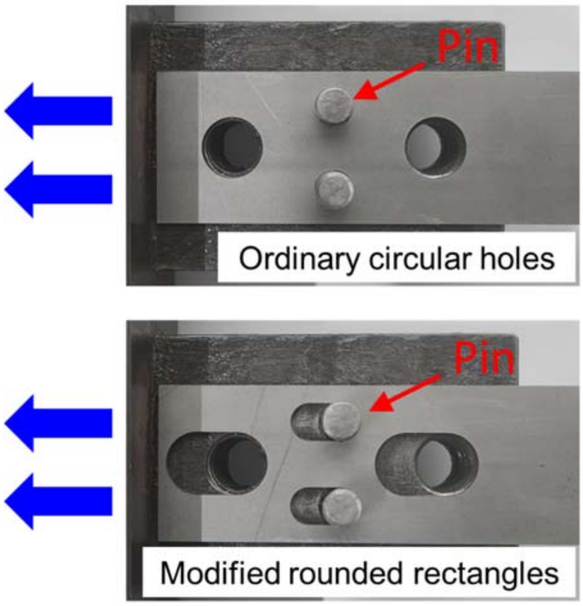

Fig. 11. Modification of the grip condition.

The AOI-averaged velocity, strain rate and acceleration in the loading direction of the original and modified grips were compared, as shown in Fig. 12. Interestingly, the strain rate after modification increased abruptly and remained comparatively steady and the acceleration magnitude increased remarkably. Notably, the velocity and acceleration were not raised more when the sliding distance was elongated from 6 to 9 mm for the modified grips.

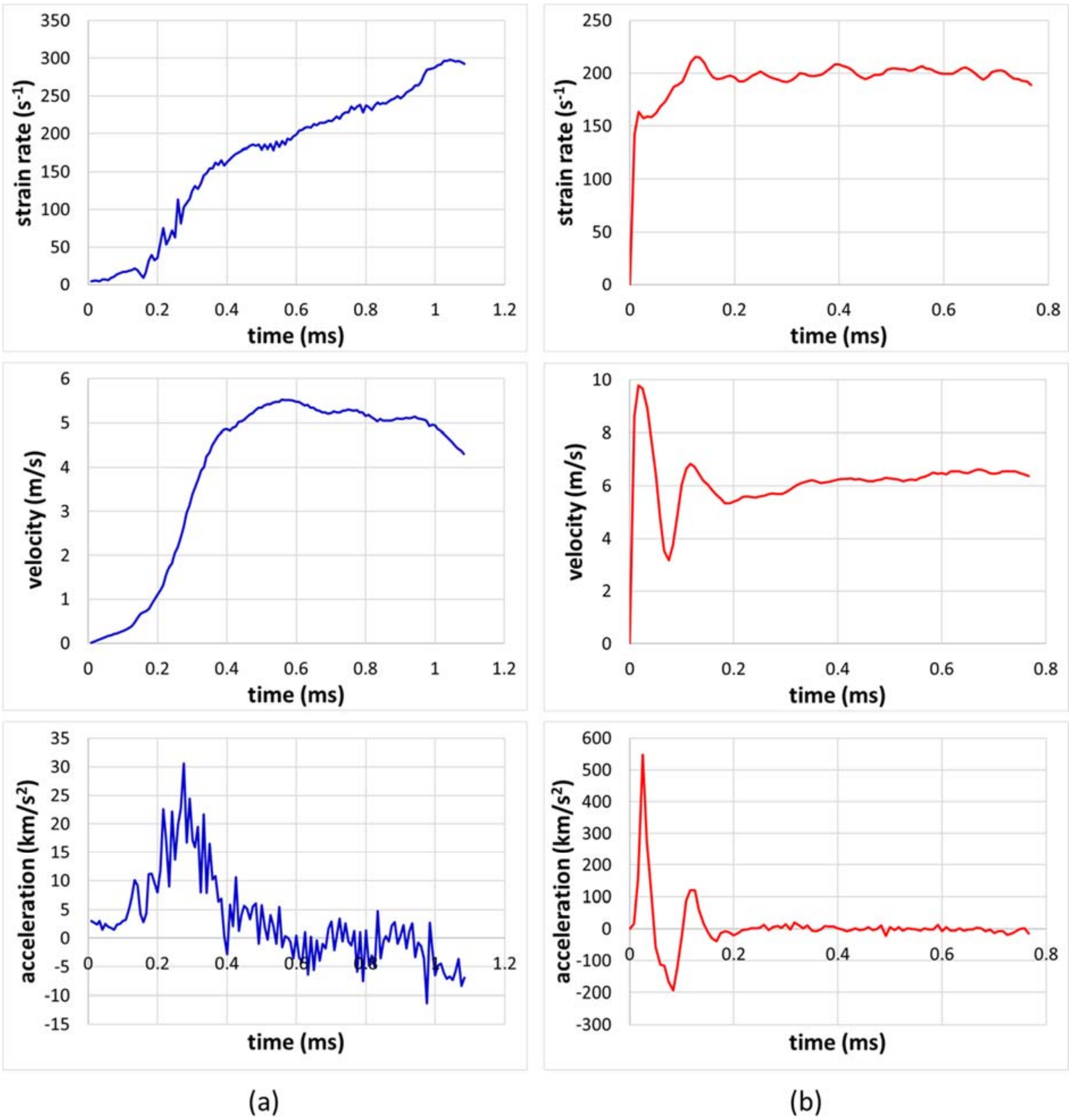

Fig. 12. Comparison of AOI-averaged strain rates, velocities and accelerations (a) circular holes (b) rounded rectangles.

In addition, one rounded rectangle was used for another geometrical configuration to raise the acceleration magnitude, as depicted in Fig. 13(a). The pin diameter was extended from 7 to 12 mm as it was thought that a stronger strike would raise the acceleration magnitude. However, the resulting strain rate behavior, Fig. 13(b), exhibited a sudden decrease early on because the stronger strike due to the high velocity of the pin crumpled the edge of the rounded rectangle.

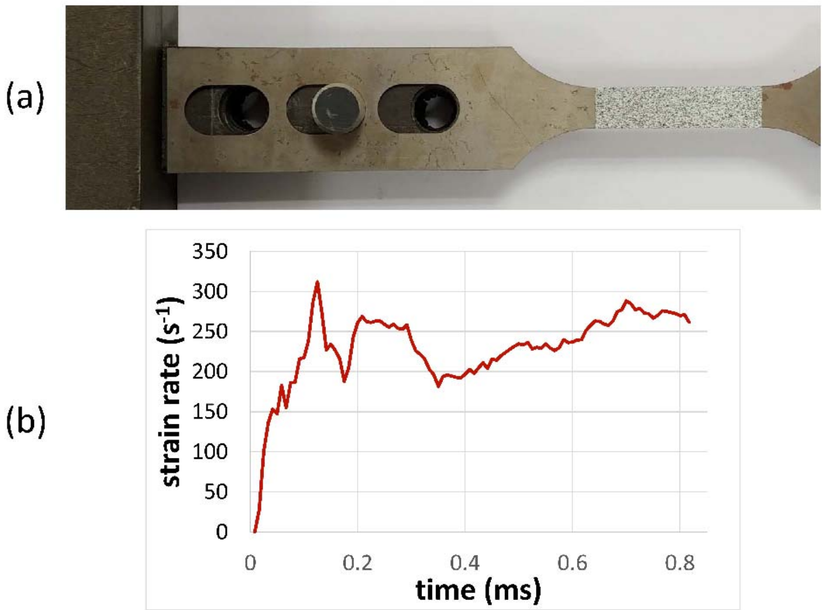

Fig. 13. (a) Another geometrical configuration for the grip condition and (b) the measured strain rate.

Therefore, a grip configuration with two pins was selected although it may provide additional vibrations during the dynamic test if the alignment between the specimen and the sliding fixture is not accurate. Thus, special attention was paid to the alignment using additional sliding guides, as shown in Fig. 14.

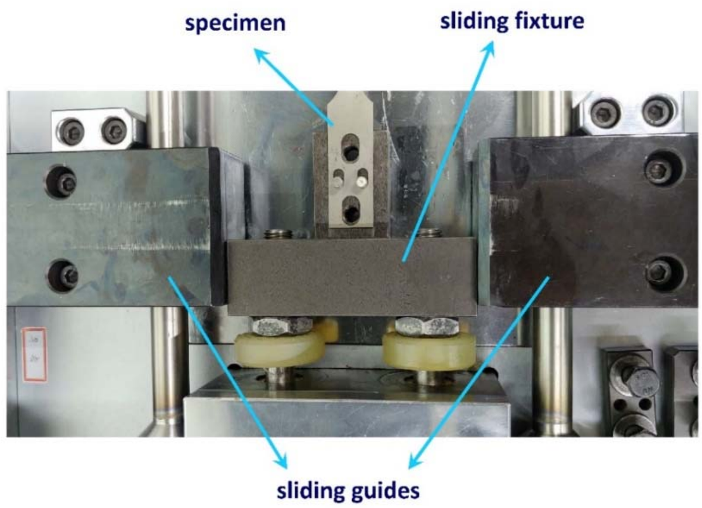

Fig. 14. Sliding guides for the alignment.

Initially, the moving crosshead in Fig. 2 was made of steel. It was found that the strain rate and velocity increased rather slowly due to a significant mass of the moving crosshead even after replacing the circular holes with rounded rectangles as shown in Fig. 15. Therefore, the material of the moving crosshead was changed from steel to duralumin and the structure of the crosshead was modified to make an empty space inside. Finally, total weight of the moving crosshead was reduced to 25 % of the original weight, resulting in a sudden deformation jump as shown in Fig. 12.

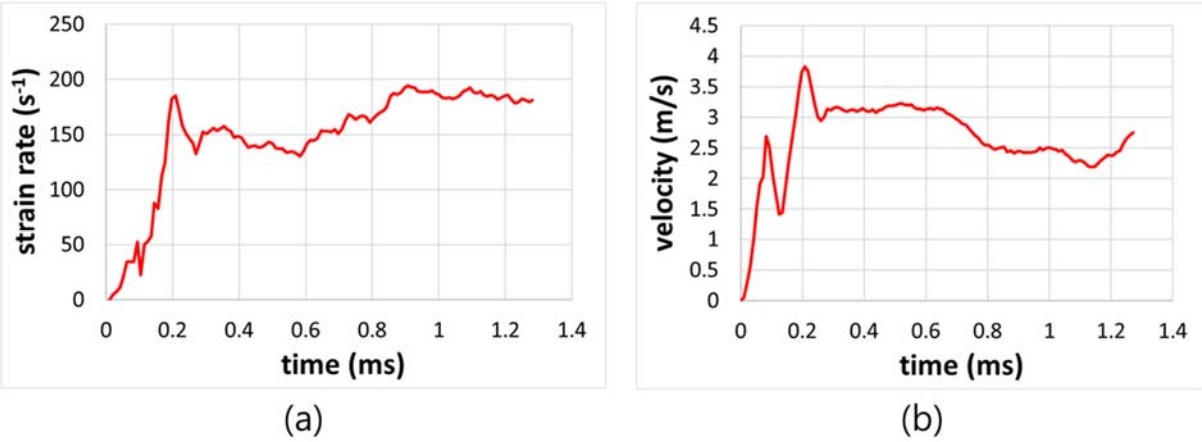

Fig. 15. Evolution of (a) AOI-averaged strain rate (b) velocity with an initial crosshead.

4.1.2 Increase of elastic strain energy

Another approach for increasing the acceleration was to increase the total elastic strain energy. As explained in Section 2.1, the mechanism of the IFHS tester is based on the energy transformation from elastic strain energy to kinetic energy. If the amount of elastic strain energy increases in the two frame bars, the kinetic energy of the specimen also increases.

The elastic strain energy (strain energy density × frame bar volume) stored in each frame bar is

$$\text{elastic strain energy} = \frac{1}{2}\sigma_{bar}\varepsilon_{bar} \times A_{bar}L_{bar} = \frac{1}{2}E_{bar}\varepsilon_{bar}^2 A_{bar}L_{bar} \quad (15)$$

where σ_{bar}, ε_{bar}, E_{bar}, A_{bar}, and L_{bar} are the stress, strain, Young's modulus, cross-sectional area, and length of the frame bar, respectively. The accumulated elastic strain energy in the frame bars is affected by their length, diameter, and material.

When the coupler is broken, the energy in the frame bar is released and converted to kinetic energy (no energy loss and constant velocity of the frame bar are assumed).

$$\text{kinetic energy} = \frac{1}{2} m_{bar} v_{bar}^2 = \frac{1}{2} (A_{bar} L_{bar} \rho_{bar}) v_{bar}^2 \tag{16}$$

where m_{bar}, ρ_{bar}, and v_{bar} denote the mass, density, and velocity of the frame bar, respectively. For an accurate calculation, the mass of the additional frame module parts was also considered in m_{bar}.

v_{bar} is the impact velocity, which can be derived from Eqs. (15) and (16).

$$\text{impact velocity } v_{bar} = \sqrt{\frac{E_{bar}}{\rho_{bar}}} \varepsilon_{bar} \tag{17}$$

The initial frame bar was made of steel, and its length and diameter were 1270 mm and 25 mm, respectively. The IFHS tester was initially designed after considering several factors, such as sufficient elastic strain energy stored in the frame bars to break the AHSS specimens and target strain rates [36,37]; however, these factors are not explained here in detail because they are beyond the scope of this study.

Eq. (17) indicates that the impact velocity is affected by the material type and the strain magnitude of the energy frame bar. The strategy was to increase the impact velocity to obtain a larger magnitude of acceleration. Accordingly, several methods were proposed to increase the impact velocity.

The first method consisted in changing the material from steel to titanium. For an applied force of 400 kN, corresponding to the coupler capacity, the theoretically calculated impact velocities given in Table 4 show that the value is higher for titanium compared to steel. In the calculation of impact velocity, the total mass of the frame bars and additional frame module parts was used. In addition, the expected strain rate in the AOI was calculated based on the following simple approximation:

$$\text{strain rate } \dot{\varepsilon} = \frac{\varepsilon}{t_e} = \frac{\frac{l}{l_0}}{t_e} = \frac{v_{bar}}{l_0} \tag{18}$$

where t_e is the elapsed time, l_0 the undeformed gauge length, and l the deformed gauge length.

Table 4

Change in impact velocity and strain rate depending on the material (25 mm diameter).

Material	Young's modulus (GPa)	Density (kg/m^3)	Stress (MPa) / strain	Impact velocity (m/s)	Strain rate (s^{-1})
Steel	200	7870	408 / 0.0020	6.74	193
Titanium	110	4500	408 / 0.0037	10.3	294

The second method was to increase the coupler capacity allowing to raise the stress and elastic strains in the frame bars, thus the amount of stored elastic strain energy in Eq. (15). However, when the capacity of the coupler was increased from 400 to 500 kN, unexpected damage occurred in other parts of the multi-components IFHS tester and this method was discarded.

The third method was to decrease the diameter of the two energy frame bars to induce a higher impact velocity. When the applied force was the same, the stress and strain levels of the frame bars increased with decreasing diameter, resulting in an increase of the impact velocity, as shown in Eq. (17). Therefore, the diameter of the frame bars, initially 25 mm, was reduced to 20 mm. Table 5 compares the theoretically calculated values when the diameter of the frame bar was changed from 25 to 20 mm. With a diameter reduction of 5 mm, the elastic strain energy increased significantly enough to change the impact velocity from 10.3 m/s to 13.8 m/s.

Although the impact velocity theoretically increases with the amount of kinetic energy, it may not translate into acceleration, which is the slope of the velocity–time graph. This aspect should be verified experimentally.

Table 5

Change in impact velocity depending on the diameter (Titanium bar).

Diameter of frame bar	25 mm	20 mm
Coupler capacity	400 kN	
Stress / strain	408 MPa / 0.0037	637 MPa / 0.0058
Strain energy density	755 kJ/m^3	1,850 kJ/m^3
Total strain energy	941 J	1473 J
Impact velocity	10.3 m/s	13.8 m/s

For this purpose, a 1.2 mm thick dual-phase DP980 steel sheet specimen was investigated. Dynamic tensile tests were carried out with the IFHS tester using the frame bars of diameters 25 and 20 mm. The AOI-averaged velocity and acceleration were calculated from the displacements and are shown in Fig. 16. The average velocity increased from approximately 6 to 9 m/s, and the maximum acceleration increased by approximately 300 km/s^2, from 568 to 899 km/s^2, after the change in diameter.

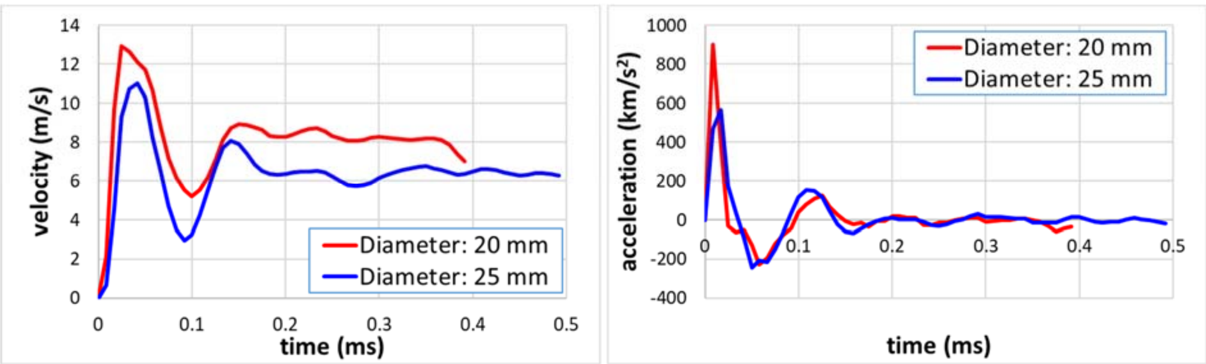

Fig. 16. Comparison of measured velocity and acceleration between the diameters of 25 mm and 20 mm.

As observed from the simulation results, the Johnson–Cook model parameter was identified correctly using only acceleration when the maximum acceleration magnitude was approximately 1.0×10^3 km/s^2. Interestingly, the experimental maximum acceleration magnitude for the diameter of 20 mm was close to the target maximum acceleration magnitude from the simulation.

In addition, the evolution of strain and acceleration distribution over the area of interest of the specimen for the diameter of 20 mm is shown in Figs. 17, 18, and 19. The distribution is shown in undeformed configuration for the sake of comparison. Each contour map corresponds to the step with a number shown in the acceleration curve in Fig. 17. It was found that the acceleration distribution is very heterogeneous over the AOI and local acceleration magnitude is higher than 1,000 km/s^2 in some triangular elements. The acceleration information starts to disappear at around 0.15 ms. It is worth noting here that the average strain reaches about 4.5 % at around 0.15 ms.

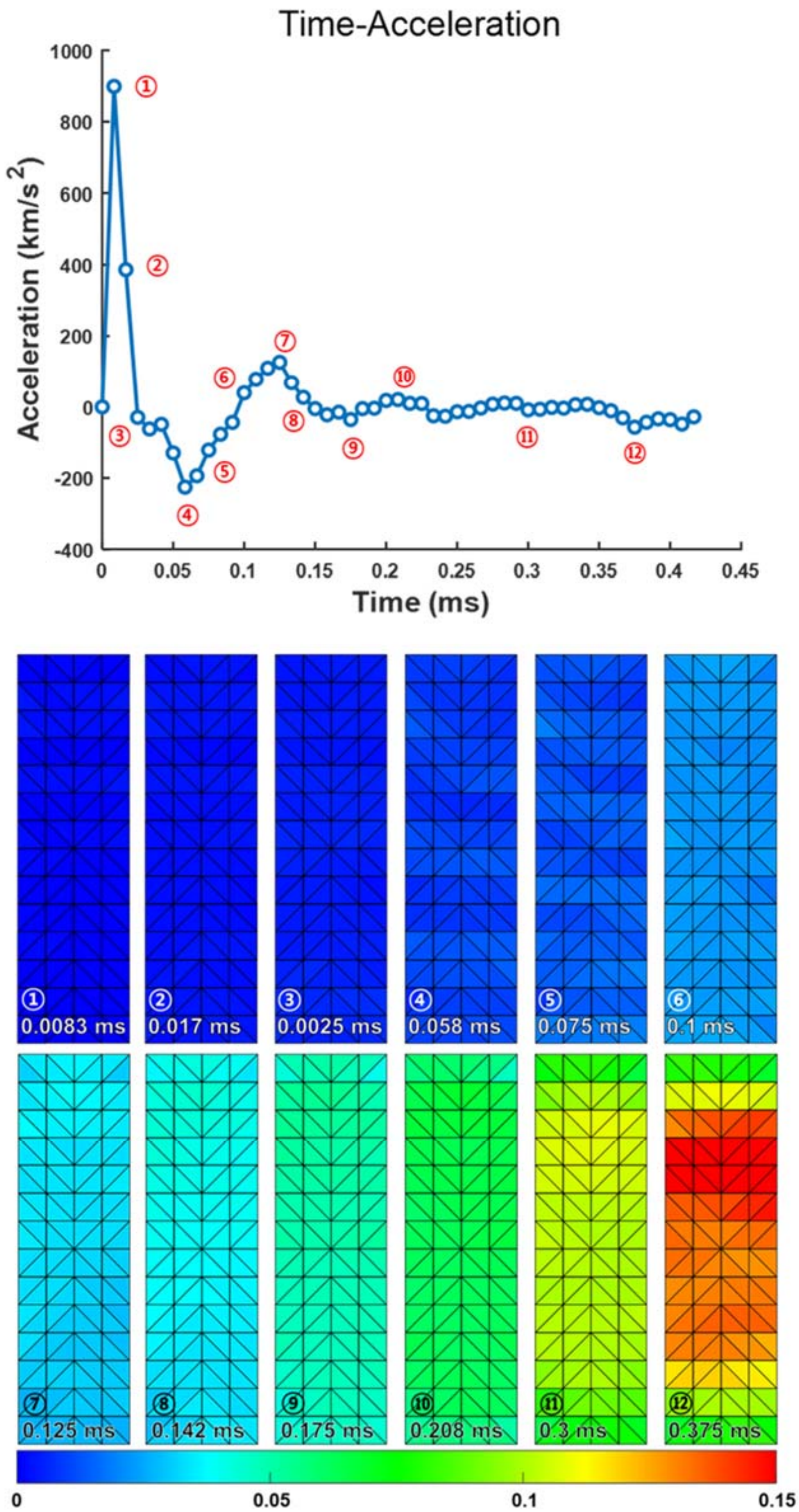

Fig. 17. Evolution of strain distribution over the area of interest for the diameter of 20 mm.

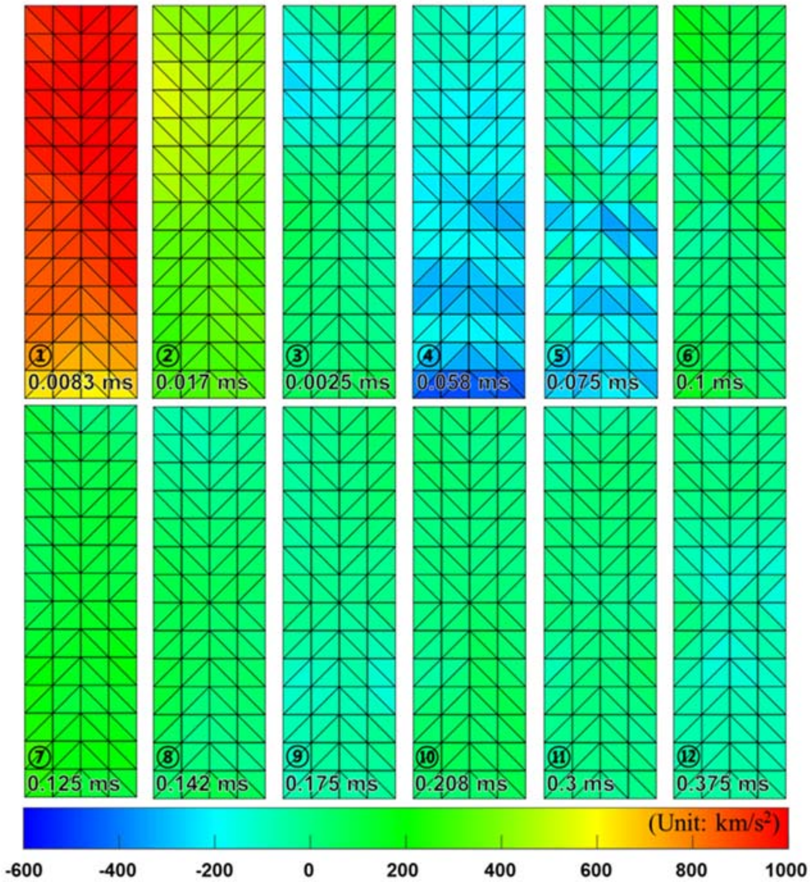

Fig. 18. Evolution of acceleration distribution over the area of interest for the diameter of 20 mm (with the same scale bar).

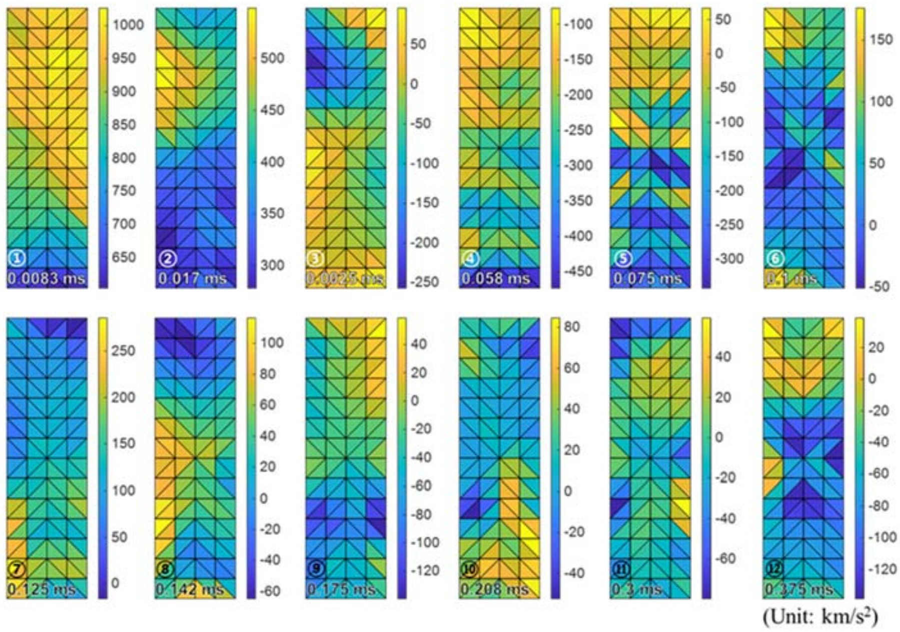

Fig. 19. Evolution of acceleration distribution over the area of interest for the diameter of 20 mm (with different scale bars).

The average strain rate for the bar diameter of 20 mm also increased (to approximately 350 s^{-1}) compared with that for the diameter of 25 mm (approximately 300 s^{-1}), as shown in Fig. 20. The decrease in strain rate at around 50 microseconds is probably due to the dynamics of the contact between the pin and rounded rectangle (loss of contact for a small time, like a rebound).

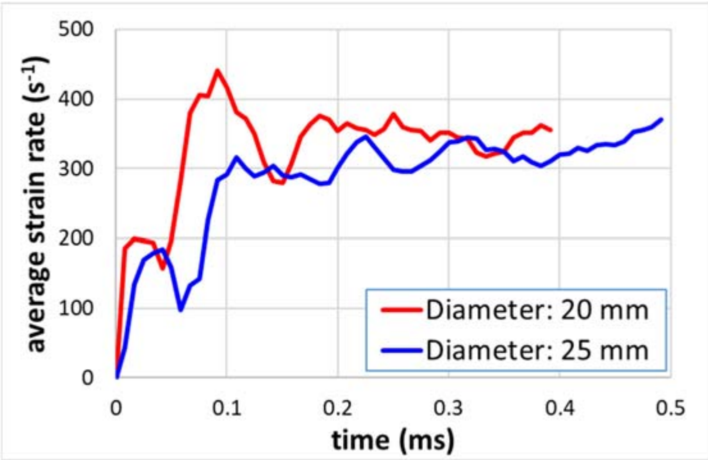

Fig. 20. Comparison of average strain rate between the diameters of 25 mm and 20 mm.

It is worth noting here that the acquisition frame rate is important for capturing the deformation in a high-speed dynamic test. In this study, a rate of 120,000 frames per second (fps) was selected with a spatial sampling of 640 × 128 pixels. However, based on Fig. 16, this rate appeared insufficient to define the peak velocity accurately. Therefore, the actual maximum acceleration might have been higher than the apparent measured value. Since the important acceleration data is provided in the initial deformation stage of very short duration in the IFHS test, the high-speed camera fps should be increased as much as possible to prevent information loss [38]. However, an increase of the fps value is accompanied by a decrease of the spatial sampling owing to the characteristics of the high-speed camera which, in turn, results in a higher noise level affecting the identification. Therefore, a compromise between the spatial and temporal resolutions is required.

4.2 Standard quasi-static uniaxial tensile tests

Quasi-static uniaxial tension tests were performed with ASTM E8 tensile specimens. Engineering stress–strain curves were obtained at a strain rate of 0.002 s^{-1}. The 0.2 % offset method was applied to calculation of the true stress–plastic strain curves σ_r in Eq. (10). The curves were fitted using various hardening laws and the best turned out to be a combination of the Swift and modified Voce hardening [27].

$$\sigma_r = X_1\left(X_2 + \varepsilon_p\right)^{X_3} + X_4 + X_5\varepsilon_p + X_6\left(1 - \exp\left(-X_7\varepsilon_p\right)\right) \quad (19)$$

The hardening parameters, determined through a standard optimization procedure, are listed in Table 6. A maximum uniform plastic strain of 4.1 % was achieved for the DP980 steel sheet.

Table 6

Hardening parameters of DP980 at quasi-static (units for X_1, X_4, X_5, X_6: MPa).

X_1	X_2	X_3	X_4	X_5	X_6	X_7
640.4	0.0001022	0.1328	530.9	101.4	143.5	149.9

4.3 Acquisition of load data in the dynamic tests

For load acquisition, strain gauges were bonded to the grip area of the specimen, where the deformation was linearly elastic. As shown in Fig. 3, the grip end at the fixed side is longer than the other grip end to provide space for strain gauges and this area is also wider to ensure that only elastic deformation occurs during the test. In order to measure the pure material response at the strain gauges attached on the specimen, the plastic stress wave front generated in the specimen gauge area should reach the strain gauges before the reflected elastic stress wave front at the end of transmitter bar arrives at the strain gauges [28,36]. The length of the transmitter bar was determined based on a calculation method in [28] to avoid the effect of the reflected stress wave. The calculated minimum length of transmitter bar was 275 mm in this study and the length of 600 mm was chosen finally for the sake of safety.

Vibration of the specimen was observed in the normal direction to the sheet plane. Therefore, strain gauges were bonded on each side of the specimen (front and back) to eliminate the bending effects [27]. The elastic strain was determined by averaging the voltage signals of the two gauges. The load F was calculated on the basis of Hooke's law and the cross-sectional area

$$F = AE\varepsilon \tag{20}$$

with a Young's modulus E of 209.7 GPa for DP980, as determined from the quasi-static condition. Synchronized load data was acquired from the strain gauges using a data acquisition (DAQ) system when speckle pattern images were taken by a high-speed camera.

4.4 Experimental results with the VFM

Dynamic tensile tests were conducted with three DP980 specimens for each case (bar diameters of 25 and 20 mm). To check the reproducibility, the measured velocity profiles as a function of time of the three specimens for 20 mm bar diameter are shown in Fig. 21. It can be seen that the reproducibility is reasonable, so the specimen data with the highest maximum acceleration was used for the VFM identification for each case. All the experimental data presented previously was fed into the VFM routines to identify the Johnson–Cook dynamic parameter *C*. The value of the initial estimate to initiate the identification process was found to be irrelevant to determine the global optimum within the interval [0.0001, 0.3]. The dynamic coefficient identification took less than 5 minutes.

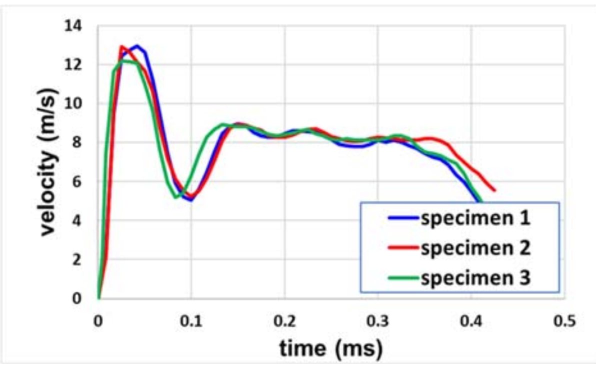

Fig. 21. Velocity profiles as a function of time of three specimens for 20 mm bar diameter.

In the case of the 25 mm bar diameter, the identification using the acceleration data only was not successful owing to the insufficient acceleration magnitude. The identified flow curve with acceleration at the strain rate of 300 s^{-1} led to flow stresses close to the quasi-static curve. For 20 mm bar diameter, the load and acceleration data were obtained simultaneously from the same experiment but the Johnson–Cook coefficient was identified using the acceleration data only or the load data only. The parameters identified with the two methods are listed in Table 7. The curve obtained with the acceleration data at the strain rate of 300 s^{-1} was compared with the curve from the load data in Fig. 22. It can be observed that the two curves are almost identical.

Table 7

Identified Johnson–Cook parameters (for the diameter of 20 mm).

From load only	From acceleration only
0.0069	0.0066

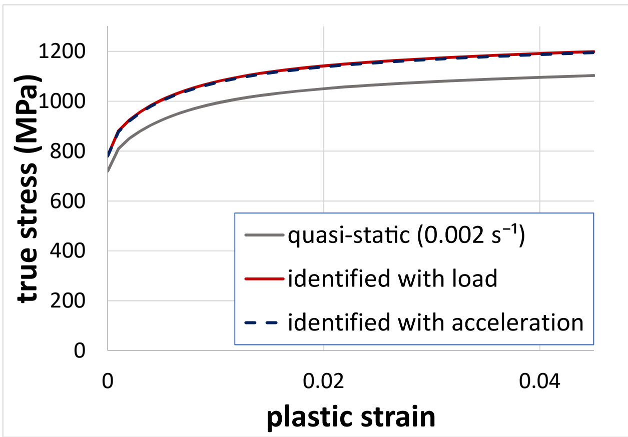

Fig. 22. Identified stress–strain curves at the strain rate of 300 s^{-1} (for the diameter of 20 mm).

The curve obtained with the acceleration data at the strain rate of 300 s^{-1} was compared with the curve from the load data using the VFM in Fig. 22. It can be observed that the two curves are almost identical. Also, comparison with the curve obtained from the raw load data using 0.2 % offset method (similar in a quasi-static test) is shown in Fig. 23. Though the stress-strain curve from the raw load data is a bit fluctuating, two curves are in reasonable agreement.

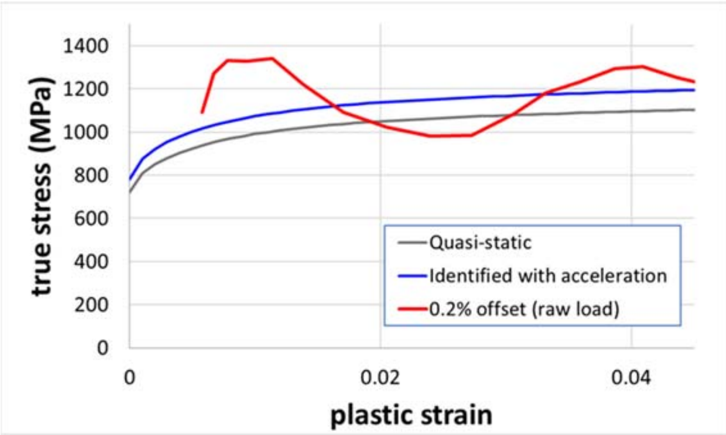

Fig. 23. Identified stress–strain curves at the strain rate of 300 s^{-1} (for the diameter of 20 mm) and comparison with the stress-strain curve from the raw load data.

In addition, for further validation of the identified Johnson–Cook parameter using acceleration information, the determined curve with Johnson–Cook model at the strain rate of 200 s^{-1} is compared with the true stress-plastic strain curve obtained from an Instron servo-hydraulic high-speed tensile tester at the strain rate of 200 s^{-1} in Fig. 24 (POSCO provided the curve data). Though the initial region including the initial yield stress shows some discrepancy because a load curve smoothing technique was applied to the servo-hydraulic tester data, it can be seen that the general trend of flow stress is very similar to each other which indicates that the identification result obtained using the VFM with the acceleration data is reliable.

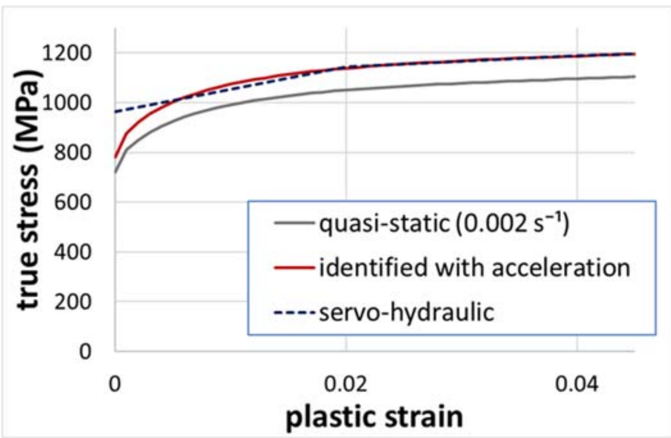

Fig. 24. Comparison of stress–strain curves at the strain rate of 200 s^{-1} between the current method and a servo-hydraulic high-speed tensile tester.

5. Limitations

In this section, some limitations of the current approach will be discussed.

5.1. Duration time of acceleration information

In this study, various techniques have been applied to increase the acceleration during the experiments because it was found from FE simulations that a critical magnitude of acceleration is required for the identification using the VFM. The maximum acceleration increased significantly up to 899 km/s^2 after applying various techniques in the experiments, leading to successful identification of Johnson–Cook parameter. However, it should be noted that not only sufficient acceleration magnitude but also sufficient duration time of acceleration is important for the identification.

The acceleration information starts to disappear at around 0.15 ms for the diameter of 20 mm in Fig. 25(a), indicating no information is present for the identification after 0.15 ms, which may result in poor identifiability. In this study, an advanced high-strength steel, DP980 was chosen and the maximum strain (at maximum strength) of DP980 at quasi-static is around 4~5 %. As can be seen in Fig. 25(b), the strain level is around 4.5 % at around 0.15 ms. Therefore, it is considered that the duration time of acceleration is sufficient for the identification of strain rate dependence of DP980 in this study.

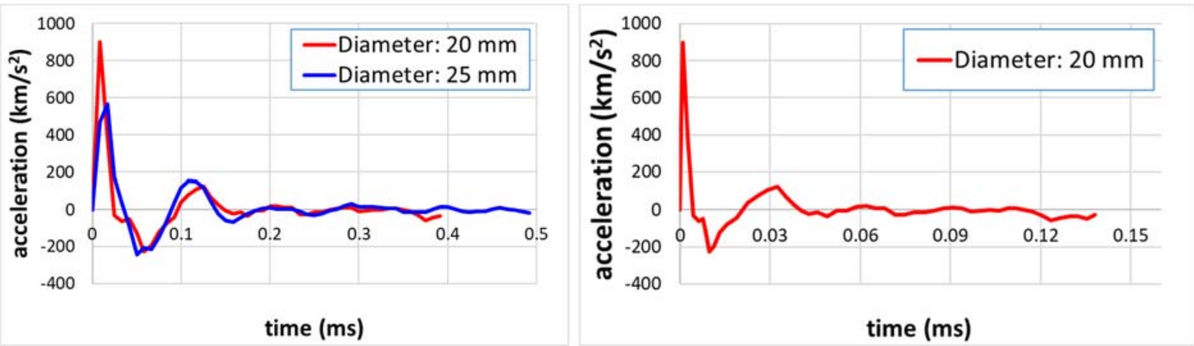

Fig. 25. Evolution of the acceleration (a) as a function of time (b) as a function of strain for the diameter of 20 mm.

Nonetheless, there are various types of advanced high-strength steel which have longer elongation as shown in Fig. 26. Therefore, in order to provide good identifiability, methods of increasing the duration time of acceleration information will have to be investigated in more depth.

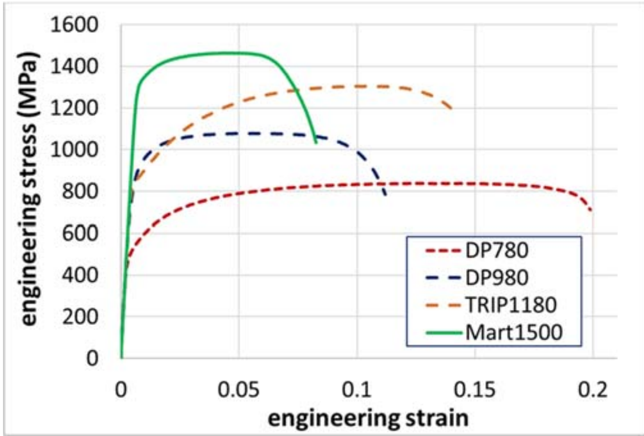

Fig. 26. Engineering stress-strain curves of various AHSSs at quasi-static.

5.2. Spatial and temporal resolution

As described in section 4.1.1, temporal and spatial resolutions are important parameters affecting precision of the current approach. In this study, a rate of 120,000 fps was selected with a spatial sampling of 640 × 128 pixels. It was observed that the current fps appeared insufficient to measure the maximum acceleration accurately. This issue can be overcome with the usage of an ultra-high-speed camera, which is very costly.

Therefore, a compromise between the spatial and temporal resolutions was obtained with the current experimental set-up including the high-speed camera. However, an optimal setting for the spatial and temporal resolutions is not straightforward because several factors should be considered such as maximum acceleration related to temporal resolution, strain rate information and experimental noise level related to spatial resolution. The goal of this study was to determine the strain rate dependence at intermediate strain rates using acceleration information. If the purpose is just to increase the acceleration magnitude, the AOI size can be reduced with a higher frame rate and smaller spatial sampling size as shown in Fig. 27. For the case of × 0.65 times in section 3.1, indeed, the maximum acceleration increased in the cases of AOI 2 and AOI 3 as shown in Fig. 28. However, none of the three cases (AOI 2, AOI 3, and AOI 4) resulted in correct identification. As discussed in [27], rich strain rate information should be provided to identify strain rate dependence with a proper rate dependent model using the VFM. It is considered that strain rate information is not sufficient for determination of strain rate dependence in the three cases.

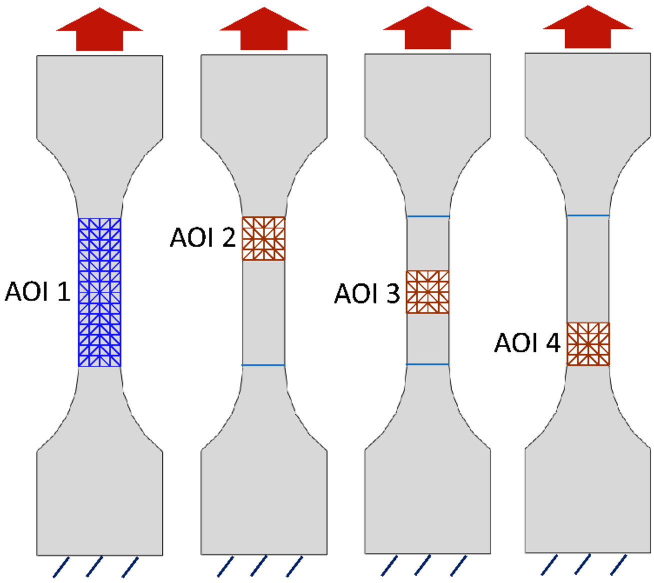

Fig. 27. Different AOI size and location.

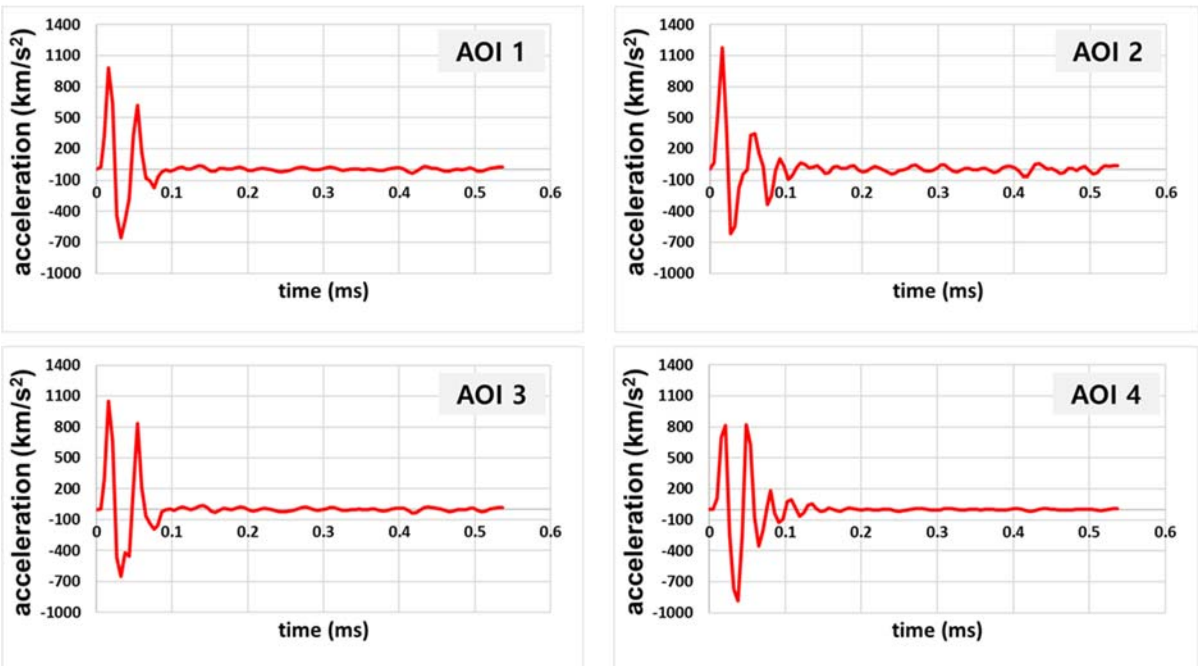

Fig. 28. AOI-averaged acceleration evolution for the case of × 0.65 in section 3.1.

Current spatial and temporal resolutions were chosen based on trial and error. It should be investigated further to make optimal settings for spatial and temporal resolutions in the current measurement technique more systematically. This issue can be handled using a simulator as presented in [39].

5.3 Control of coupler capacity

As explained in section 2.1, the current IFHS tensile equipment utilizes the elastic strain energy stored in frame bars to generate high-speed impact pulses. The accumulated elastic strain energy is controlled by the coupler capacity. Though the reproducibility of couplers is good as shown in Fig. 21, it is very tricky to control the coupler capacity accurately, thus speed, strain rate, and acceleration. The coupler has the form of a cylinder with a notch at the center, so the coupler capacity is determined by the notch depth. Therefore it is required to measure the coupler capacity by changing the notch depth based on trial and error. An alternative would be electromagnetic devices which can replace the coupler.

6. Conclusion

The stress–strain information from intermediate strain rates is essential input to obtain reliable crash simulation results. However, the load applied is not easy to measure accurately at intermediate or high strain rates, owing to the inertial effect. A new methodology was applied in this study, to obtain the dynamic curve of a sheet metal specimen at an intermediate strain rate without measuring the loads. This study utilized the VFM to obtain the dynamic parameters of the Johnson–Cook model with acceleration information. A modified high-speed tensile equipment for steel sheet specimens was devised to increase the acceleration magnitude, and the dynamic behavior was characterized using a DIC technique with a high-speed camera. The stress–strain curve of a dual-phase DP980 steel sheet at an intermediate strain rate of 300 s^{-1} was obtained from the acceleration information. The main observations of this study are as follows:

(1) Before the actual experiments, FE simulations using Abaqus were performed to determine the feasibility of the identification from the acceleration data. To check the minimum acceleration magnitude required for the identification, the velocity boundary condition extracted from real experimental results with the IFHS tester was adjusted to increase the acceleration magnitude. The identification was successful with the current test configuration when the maximum acceleration magnitude was approximately 1.0×10^3 km/s^2.

(2) A modified high-speed tensile equipment for steel sheet specimens was developed to increase the magnitude of the acceleration during the experiments. Various techniques have been applied to increase the acceleration. It was found that the most reliable method to increase the stored elastic strain energy, based on the mechanism, was to employ titanium frame bars of 20 mm diameter. The higher strain energy increased the impact velocity, resulting in a higher acceleration. The maximum acceleration magnitude increased from 568 km/s^2 to 899 km/s^2.

(3) The identification of the Johnson–Cook parameter with the acceleration was not successful when the energy frame bars with 25 mm diameter were used because of insufficient acceleration. However, the stress–strain curve based on the acceleration data was very close to the curve obtained from the load for the diameter of 20 mm at 300 s^{-1} strain rate, owing to the increased acceleration magnitude. This indicates that the identification result obtained using the VFM with acceleration is reliable.

Acknowledgment

The authors are grateful for the generous support provided by POSCO.

References

[1] W. R. Whittington, A. L. Oppedal, D. K. Francis, and M. F. Horstemeyer, "A novel intermediate strain rate testing device: The serpentine transmitted bar," *Int. J. Impact Eng.*, vol. 81, pp. 1–7, Jul. 2015, doi: 10.1016/J.IJIMPENG.2015.02.009.

[2] T. Bhujangrao, C. Froustey, E. Iriondo, F. Veiga, P. Darnis, and F. G. Mata, "Review of Intermediate Strain Rate Testing Devices," *Metals (Basel).*, vol. 10, no. 7, p. 894, 2020.

[3] H. Huh, J. H. Lim, S. B. Kim, S.-S. Han, and S. H. Park, "Formability of the steel sheet at the intermediate strain rate," in *Key Engineering Materials*, 2004, vol. 274, pp. 403–408.

[4] A. Yoshitake, K. Sato, and Y. Hosoya, "A study on improving crashworthiness of automotive parts by using high strength steel sheets," 1998.

[5] K. Mahadevan, P. Liang, and J. Fekete, "Effect of strain rate in full vehicle frontal crash analysis," *SAE Trans.*, pp. 863–871, 2000.

[6] H. Huh, J. H. Lim, J. H. Song, K. S. Lee, Y. W. Lee, and S. S. Han, "Crashworthiness assessment of side impact of an auto-body with 60TRIP steel for side members," *Int. J. Automot. Technol.*, vol. 4, no. 3, pp. 149–156, 2003.

[7] J. E. Field, S. M. Walley, W. G. Proud, H. T. Goldrein, and C. R. Siviour, "Review of experimental techniques for high rate deformation and shock studies," *Int. J. Impact Eng.*, vol. 30, no. 7, pp. 725–775, 2004.

[8] T. R. Kaliat, *High Rates and Impact Experiments*. Springer handbook of experimental solid mechanics, 2008.

[9] M. Borsutzki, D. Cornette, Y. Kuriyama, A. Uenishi, B. Yan, and E. Opbroek, "Recommendations for dynamic tensile testing of sheet steels," *Int. iron steel Inst.*, vol. 30, 2005.

[10] F. Pierron, M. A. Sutton, and V. Tiwari, "Ultra high speed DIC and virtual fields method

analysis of a three point bending impact test on an aluminium bar," *Exp. Mech.*, vol. 51, no. 4, pp. 537–563, 2011.

[11] H. Huh, J. H. Lim, and S. H. Park, "High speed tensile test of steel sheets for the stress-strain curve at the intermediate strain rate," *Int. J. Automot. Technol.*, vol. 10, no. 2, pp. 195–204, 2009.

[12] D. M. Bruce, D. K. Matlock, J. G. Speer, and A. K. De, "Assessment of the strain-rate dependent tensile properties of automotive sheet steels," 2004.

[13] M. Zrida *et al.*, "High-speed tensile tests on a polypropylene material," *Polym. Test.*, vol. 29, no. 6, pp. 685–692, 2010.

[14] Y. Xia, J. Zhu, K. Wang, and Q. Zhou, "Design and verification of a strain gauge based load sensor for medium-speed dynamic tests with a hydraulic test machine," *Int. J. Impact Eng.*, vol. 88, pp. 139–152, 2016.

[15] X. Xiao, "Dynamic tensile testing of plastic materials," *Polym. Test.*, vol. 27, no. 2, pp. 164–178, 2008.

[16] R. Moulart, F. Pierron, S. R. Hallett, and M. R. Wisnom, "Full-field strain measurement and identification of composites moduli at high strain rate with the virtual fields method," *Exp. Mech.*, vol. 51, no. 4, pp. 509–536, 2011.

[17] F. Pierron and P. Forquin, "Ultra-high-speed full-field deformation measurements on concrete spalling specimens and stiffness identification with the virtual fields method," *Strain*, vol. 48, no. 5, pp. 388–405, 2012.

[18] F. Pierron, H. Zhu, and C. Siviour, "Beyond Hopkinson's bar," *Philos. Trans. R. Soc. A*, vol. 372, p. 20130195, 2014.

[19] M. Grediac, F. Sur, and B. Blaysat, "The Grid Method for In-plane Displacement and Strain Measurement: A Review and Analysis," *Strain*, vol. 52, no. 3, pp. 205–243, 2016.

[20] F. Pierron and M. Grediac, *The virtual fields method: Extracting constitutive mechanical parameters from full-field deformation measurements*. Springer New York, 2012.

[21] G. Le Louëdec, F. Pierron, M. A. Sutton, C. Siviour, and A. P. Reynolds, "Identification of the dynamic properties of Al 5456 FSW welds using the virtual fields method," *J. Dyn. Behav. Mater.*, vol. 1, no. 2, pp. 176–190, 2015.

[22] B. Koohbor, A. Kidane, M. A. Sutton, X. Zhao, and S. Mallon, "Analysis of dynamic bending test using ultra high speed DIC and the virtual fields method," *Int. J. Impact Eng.*, vol. 110, pp. 299–310, 2017.

[23] P. Bouda, B. Langrand, D. Notta-Cuvier, E. Markiewicz, and F. Pierron, "A computational approach to design new tests for viscoplasticity characterization at high strain-rates," *Comput. Mech.*, vol. 64, no. 6, pp. 1639–1654, 2019.

[24] T. Fourest *et al.*, "Image-based inertial impact test for characterisation of strain rate dependency of Ti6al4v titanium alloy," *Exp. Mech.*, vol. 60, no. 2, pp. 235–248, 2020.

[25] L. Fletcher, F. Davis, S. Dreuilhe, A. Marek, and F. Pierron, "High strain rate elasto-plasticity identification using the image-based inertial impact (IBII) test part 2: Experimental validation," *Strain*, vol. 57, no. 2, p. e12374, 2021.

[26] D. Leem, J. H. Kim, F. Barlat, J. H. Song, and M. G. Lee, "Identification of Dynamic Flow Stress Curves Using the Virtual Fields Methods: Theoretical Feasibility Analysis," *Met. Mater. Int.*, vol. 24, no. 2, pp. 351–361, Mar. 2018, doi: 10.1007/s12540-018-0024-8.

[27] J.-S. Park, J.-M. Kim, F. Barlat, J.-H. Lim, F. Pierron, and J.-H. Kim, "Characterization of dynamic hardening behavior at intermediate strain rates using the virtual fields method," *Mech. Mater.*, vol. 162, p. 104101, 2021.

[28] T. K. Tran and D. J. Kim, "Strain energy frame impact machine (SEFIM)," *J. Adv. Concr. Technol.*, vol. 10, no. 3, pp. 126–136, 2012, doi: 10.3151/jact.10.126.

[29] M. A. Sutton, J. J. Orteu, and H. Schreier, *Image correlation for shape, motion and deformation measurements: basic concepts, theory and applications*. Springer Science & Business Media, 2009.

[30] E. M. C. Jones, M. A. Iadicola, and others, "A good practices guide for digital image

correlation," *Int. Digit. Image Correl. Soc.*, vol. 10, 2018, doi: https://doi.org/10.32720/idics/gpg.ed1/print.format.

[31] S. Avril, P. Feissel, F. Pierron, and P. Villon, "Comparison of two approaches for differentiating full-field data in solid mechanics," *Meas. Sci. Technol.*, vol. 21, no. 1, p. 15703, 2009.

[32] D. C. Lay, *Linear algebra and its applications*. Pearson Education India, 2003.

[33] POSCO, "Automotive Steel Data Book," 2014. [Online]. Available: http://product.posco.com.

[34] M. Grédiac and F. Pierron, "Applying the virtual fields method to the identification of elasto-plastic constitutive parameters," *Int. J. Plast.*, vol. 22, no. 4, pp. 602–627, 2006.

[35] M. A. Sutton, X. Deng, J. Liu, and L. Yang, "Determination of elastic-plastic stresses and strains from measured surface strain data," *Exp. Mech.*, vol. 36, no. 2, pp. 99–112, 1996.

[36] D. J. Kim, K. Wille, S. El-Tawil, and A. E. Naaman, "Testing of cementitious materials under high-strain-rate tensile loading using elastic strain energy," *J. Eng. Mech.*, vol. 137, no. 4, pp. 268–275, 2011.

[37] T. K. Tran and D. J. Kim, "Strain energy frame impact machine (SEFIM)," *J. Adv. Concr. Technol.*, vol. 10, no. 3, pp. 126–136, 2012.

[38] J. H. Kim, G. A. Lee, and M. G. Lee, "Determination of Dynamic Strain Hardening Parameters Using the Virtual Fields Method," *Int. J. Automot. Technol.*, vol. 16, no. 1, pp. 145–151, 2015, doi: 10.1007/s12239−015−0016−3.

[39] M. Rossi and F. Pierron, "On the use of simulated experiments in designing tests for material characterization from full-field measurements," *Int. J. Solids Struct.*, vol. 49, no. 3–4, pp. 420–435, 2012.